

Thermal conductivity suppression in bismuth nanowires

Arden L. Moore,¹ Michael T. Pettes,¹ Feng Zhou,² and Li Shi^{1,2,a)}

¹Department of Mechanical Engineering, The University of Texas at Austin, Austin, Texas 78712, USA

²Materials Science and Engineering Program, Texas Materials Institute, The University of Texas at Austin, Austin, Texas 78712, USA

(Received 11 May 2009; accepted 24 June 2009; published online 11 August 2009)

The thermal conductivity of individual bismuth nanowires was characterized using a suspended microdevice and correlated with the crystal structure and growth direction obtained by transmission electron microscopy on the same nanowires. Compared to bulk bismuth in the same crystal direction perpendicular to the trigonal axis, the thermal conductivity of a single-crystal bismuth nanowire of 232 nm diameter was found to be three to six times smaller than bulk in the temperature range between 100 and 300 K, and those of polycrystalline bismuth nanowires of 74–255 nm diameter are reduced by factors of 18–78 over the same temperature range. The thermal conductivity suppression in the single-crystal nanowire can be explained by a transport model that considers diffuse phonon-surface scattering, partially diffuse surface scattering of electrons and holes, and scattering of phonons and charge carriers by ionized impurities such as oxygen and carbon of a concentration on the order of 10^{19} cm⁻³. The comparable thermal conductivity values measured for polycrystalline nanowires of different diameters suggests a grain boundary scattering mean free path for all heat carriers in the range of 15–40 nm, which is smaller than the nanowire diameters. © 2009 American Institute of Physics. [DOI: [10.1063/1.3191657](https://doi.org/10.1063/1.3191657)]

I. INTRODUCTION

Bismuth (Bi) has long been a material of interest to scientists and engineers for its highly anisotropic transport properties,¹ long carrier mean free paths,² small effective mass and long electron wavelength,^{3–5} and semimetal band structure.^{1–5} In particular, Bi-based alloys have been extensively investigated for use in thermoelectric applications. The figure of merit (ZT) for a thermoelectric material is given by

$$ZT = \frac{S^2 \sigma}{\kappa} T, \quad (1)$$

where S is the Seebeck coefficient, σ is the electrical conductivity, κ is the thermal conductivity, and T is the absolute temperature.⁶ The thermal conductivity κ is comprised of contributions from phonons (κ_{ph}), electrons (κ_e), holes (κ_h), and bipolar diffusion (κ_{eh}) such that $\kappa = \kappa_{\text{ph}} + \kappa_e + \kappa_h + \kappa_{eh}$. The three transport properties, S , σ , and κ , are interdependent, making it challenging to increase ZT . Most bulk thermoelectric materials in use today have a peak ZT comparable to or less than unity and operate in a specific temperature range. For applications in the near-ambient temperature range, Bi₂Te₃ alloys are the most commonly used materials with a typical ZT value of around 0.9–1.0 near room temperature.⁶ For a thermoelectric refrigerator to have a coefficient of performance that is competitive with vapor compression units, a ZT of 3 or greater is required.⁷ This requirement has driven the investigation of new approaches including nanostructures to increasing ZT .^{8–10}

Despite having the lowest thermal conductivity of all metals except mercury, pure Bi in its bulk form is not considered a good thermoelectric material due to its semimetal band structure.^{5,11,12} The small band overlap found in bulk Bi results in nearly equal concentrations of electrons and holes, causing the electron and hole contributions to the Seebeck coefficient to cancel each other.^{1,5,11,12} As noted by Gallo *et al.*,¹ the optimum thermoelectric efficiency for bulk Bi would be realized when one type of carrier dominates the transport such as would occur with an appropriate amount of doping with antimony or tellurium. This would increase the Seebeck coefficient and suppress the bipolar contribution to the thermal conductivity, thereby increasing ZT .¹

Interest in Bi as a thermoelectric material was renewed when theoretical investigations of size effects on the transport properties of Bi and Bi-based nanostructures predicted an enhancement in ZT for one-dimensional systems such as nanowires (NWs).^{4,5,8,13} It was suggested that the thermoelectric power factor ($S^2 \sigma$) could be enhanced because of the highly asymmetric electron density of states in a Bi NW when the diameter becomes comparable to or smaller than the long (~ 50 nm) de Broglie wavelength of electrons.¹⁴ In addition, the conduction/valence band overlap found in bulk Bi is inversely proportional to the square of the NW diameter such that a semimetal to semiconductor transition could occur in a Bi NW,⁵ making it possible to break the electron-hole symmetry so as to increase the Seebeck coefficient.

Besides the quantum confinement effects, the thermoelectric properties of a NW are also influenced by classical size effects characterized by increased boundary scattering of charge and heat carriers. Bismuth is known for having unusually long charge carrier mean free paths of up to ~ 400 μm for electrons and ~ 200 μm for holes at 4.2 K and ~ 100 nm for electrons and holes at room

^{a)}Author to whom correspondence should be addressed. Electronic mail: lishi@mail.utexas.edu.

temperature,^{2,15} suggesting that boundary scattering effects could also play a significant role on the three transport properties entering into the ZT expression. While diffuse phonon-surface scattering has been found to suppress the thermal conductivity in several NW systems,^{16–18} measurement results of thermal conductivity of Bi NWs have not been reported. Moreover, while the reduction in thermal conductivity due to phonon boundary scattering in nanostructured semiconductors has been under active investigation in an effort to increase the ZT , there have been few studies of the classical size effects on the electronic contributions to the thermal conductivity of a nanostructure such as Bi NWs where the electronic contribution plays an important role.

In this work, we report the measurement of the thermal conductivity of individual Bi NWs, and examine the crystal structure-thermal conductivity relationship. In addition, transport models are used to analyze the effects of size confinement, grain boundaries, defects, and impurities on the contributions of phonons, electrons, holes, and bipolar diffusion to thermal conductivity of the measured Bi NWs.

II. SAMPLE PREPARATION AND EXPERIMENTAL PROCEDURES

Bismuth NWs were synthesized using the vapor deposition method reported by Heremans *et al.*¹⁵ Anodic alumina membranes (AAMs) of tunable pore diameters either obtained commercially or grown via the two-step anodization method^{19,20} were used as templates for the NW synthesis. After Bi deposition, the impregnated AAMs were dissolved in a solution of 2M sodium hydroxide for 30 min, followed by repeated dilution with de-ionized (DI) water until the pH of the solution was neutral. The DI water was then replaced with isopropyl alcohol three times to produce a fluidic suspension of individual Bi NWs suitable for drop casting onto the thermal measurement devices.

The suspended microdevice shown in Fig. 1(a) was used to measure the thermal conductance of individual Bi NWs bridging the two silicon nitride (SiN_x) membranes that are suspended by six SiN_x beams over a through-substrate hole. Two platinum (Pt) electrodes and a serpentine Pt resistance thermometer are patterned on each membrane. The through-substrate hole beneath the suspended membranes allows for transmission electron microscopy (TEM) characterization to be performed on the same NW used for thermal measurements. This allows for correlation of the measured thermal properties with the crystal quality and the growth direction of the NW sample. Detailed information on the NW crystal structure is especially important given the highly anisotropic nature of bulk Bi.¹

In air, Bi NWs form a highly stable surface oxide layer that makes it challenging to make Ohmic electrical contact.^{21,22} Focused electron beam or focused ion beam deposition of platinum and nickel contacts [Fig. 1(c)] were used to improve the thermal contact between the NW and the prepatterned Pt electrodes on the membrane but did not result in electrical contact.

Thermal conductance measurements of the NW samples were performed in a vacuum-pumped cryostat according to

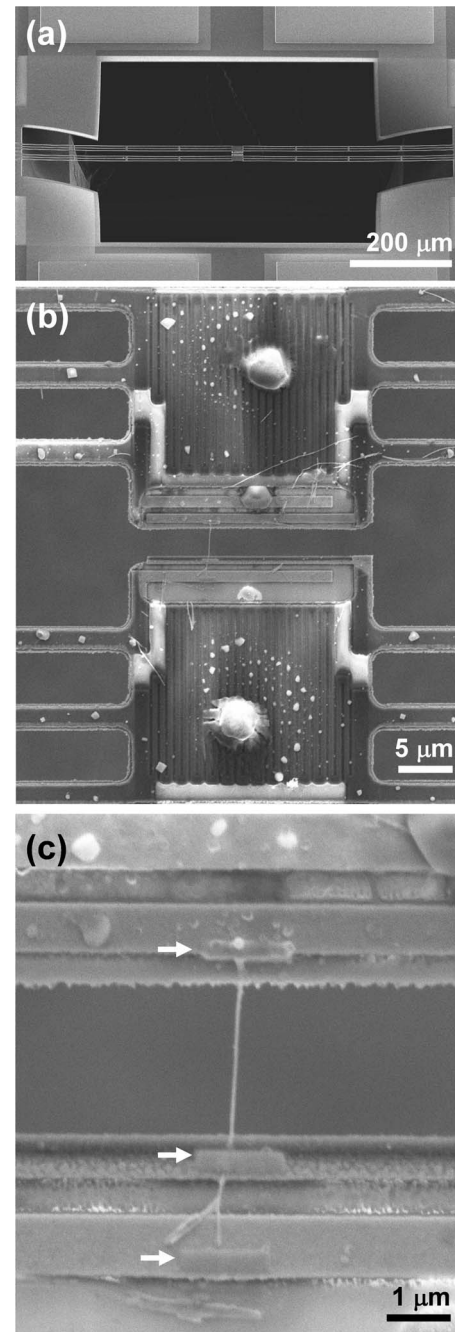


FIG. 1. (a) SEM image of the suspended microdevice. (b) SEM image of the two central membranes of the microdevice with a Bi NW trapped between the two membranes. (c) SEM image showing detail of the NW sample. The arrows indicate metal patterns deposited on the NW.

the procedure described previously.²³ In addition, a thermal conductance measurement of a blank device without a NW trapped between the two membranes was also performed. The obtained background signal measured on the blank device was attributed to heating of the substrate that has a finite spreading thermal resistance, residual gas molecules in the evacuated cryostat, and radiation. The corresponding background thermal conductance was subtracted from the measured thermal conductance of the NW samples at each corresponding temperature. For all the Bi NWs reported in this work, the background conductance was found to be at least

TABLE I. Summary of NW samples trapped on the suspended device for thermal and TEM measurement.

Sample	Outer diameter (nm)	Suspended length (μm)	Oxide (nm)	Orientation
NW1	283	9.15
NW2	255	2.56	12–35	Polycrystalline
NW3	232	3.45	10–16	$\langle 1\bar{2}0 \rangle$
NW4	157	3.38
NW5	105	2.22
NW6	74	1.61	3–4	Polycrystalline

about one order of magnitude smaller than the measured sample thermal conductance, as shown in the supplemental materials.²⁴

Upon completion of the thermal conductance measurement, TEM was used to characterize the crystal structure of samples NW2, NW3, and NW6 shown in Table I. The other three NW samples were inadvertently broken at the membrane edge when the sample was removed from the ceramic chip carrier before it could be loaded in the TEM for structure characterization. The total outer diameter and the oxide shell thickness of the Bi NW were determined by TEM measurement.

As summarized in Table I, the high resolution TEM images and electron diffraction pattern of NW3 on the suspended device [Fig. 2(a)] indicate that this Bi NW was single crystalline within the $\sim 2 \mu\text{m}$ beam spot. The growth direc-

tion of NW3 was determined to be along the $\langle 1\bar{2}0 \rangle$ crystal direction perpendicular to the trigonal axis, while NW2 and NW6 were found to be polycrystalline. Energy-dispersive x-ray spectroscopy performed on the suspended samples revealed no impurities present at detectable levels.²⁴

III. MEASUREMENT RESULTS

The thermal conductivity κ was calculated from the measured total thermal conductance G_{total} of the sample, which includes the contact thermal resistance, using the length and diameter of the suspended NW section as measured by either TEM or scanning electron microscopy (SEM). Specifically, $\kappa = G_{\text{total}}L/A_c$ where L is the length of the suspended NW segment and A_c is the cross sectional area calculated using the NW diameter. If the total outer NW diameter is used to define the cross sectional area, the obtained thermal conductivity would include the contribution from the oxide shell and would not be the same as that of the Bi core. This effective thermal conductivity of the individual bismuth nanowires including both the Bi core and the oxide shell is shown in the supplemental materials.²⁴ The thermal conductivity of amorphous bismuth oxide has not been extensively studied. We have used Slack's minimum thermal conductivity model²⁵ to estimate the thermal conductivity of the amorphous oxide shell. This gives a nearly constant value of 0.34 W/m K in the measured temperature range of between 100 and 475 K. This calculated oxide thermal conductivity was used along with the oxide shell thickness values given in Table I to calculate the thermal conductance of the oxide shell for each sample. For the three samples without TEM data, an oxide thickness of 10 nm was assumed. The resulting oxide thermal conductance was then subtracted from the measured thermal conductance. The obtained thermal conductance was used to calculate the thermal conductivity of the Bi core based on the core diameter. The difference between the oxide corrected and uncorrected thermal conductivity is in the range of 9%–14% for the measured NWs.

The measured thermal conductivity of the Bi NW core for each sample is shown in Fig. 3 along with values for bulk Bi parallel and perpendicular to the trigonal axis. The largest diameter sample, NW1 of 283 nm diameter, had the highest thermal conductivity of all samples but still below that of bulk Bi. NW3 with 232 nm diameter had a slightly smaller but still comparable thermal conductivity to NW1 in the same temperature range. However, the temperature dependence for NW3 is very weak and gives rise to much lower thermal conductivity compared to bulk at low temperatures. NW2 with 255 nm diameter and a polycrystalline structure was found to have a much lower thermal conductivity than NW3 of a single-crystal structure. For other samples with diameter below ~ 150 nm, the obtained thermal conductivity values were much smaller than bulk and showed no apparent diameter dependence.

IV. ANALYSIS

In order to understand the measured NW thermal conductivity values, the separate contributions from each heat

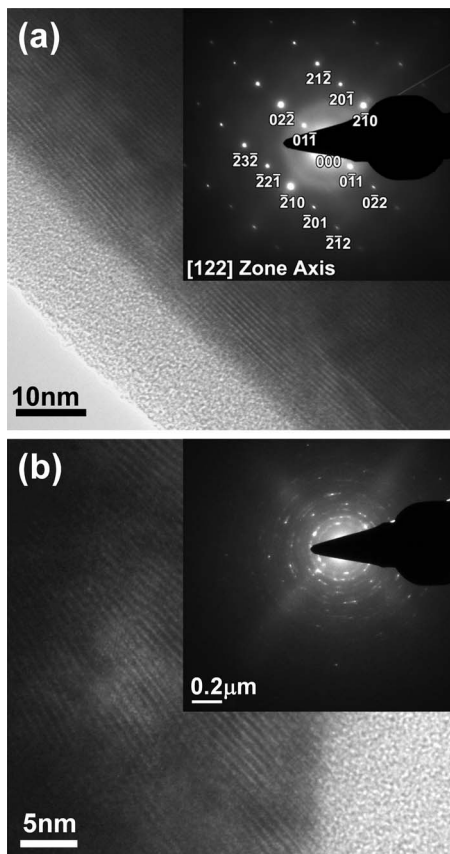


FIG. 2. High resolution TEM analysis of (a) NW3 and (b) NW2. Electron diffraction patterns using a $2 \mu\text{m}$ beam spot are shown as insets.

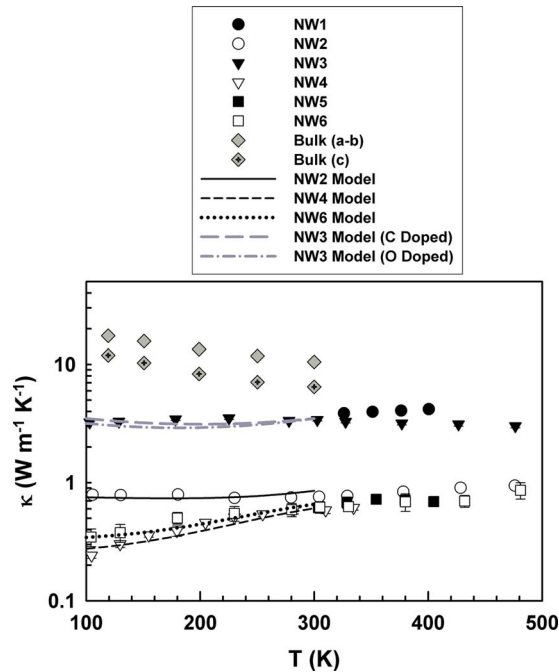


FIG. 3. (Color online) Thermal conductivity of the Bi NW cores alone. Bulk values perpendicular (*a-b* plane) and parallel (*c* axis) to the trigonal direction are taken from Ref. 1. Lines are calculation results discussed in the text.

carrier to the total thermal conductivity must be considered. For bulk Bi, it has been shown that phonons are the dominant heat carrier at low temperatures but that the electronic component ($\kappa_E = \kappa_e + \kappa_h + \kappa_{eh}$) becomes progressively more important as temperature increases.²⁶ At the Debye temperature of 120 K, about one third of the κ is attributable to κ_E .²⁶ Similarly, Gallo *et al.*¹ showed the growing importance of electronic thermal transport with increasing temperature, with κ_E accounting for about 70% of κ at 300 K perpendicular to the trigonal direction and the remaining 30% belonging to κ_{ph} .¹

To evaluate the relative contributions of the various heat carriers in the NWs and gain insight into the possible mechanisms involved in the observed thermal conductivity reduction, we have developed a model that considers thermal transport by phonons, charge carriers, and bipolar diffusion. We first model thermal transport in bulk Bi, then include additional boundary scattering and impurity/defect scattering processes for transport in the NW in order to account for the suppressed thermal conductivity.

The bulk electronic thermal transport model essentially follows the method used by Gallo *et al.*¹ to analyze bulk Bi but with more modern information regarding band parameters^{1,3,5,27,28} and carrier mobilities,²⁹ as described in detail in the supplemental materials.²⁴ We restrict our model to those temperatures for which there is bulk mobility data available, specifically in the range of 77–300 K.²⁹ The bulk lattice thermal conductivity is calculated using the modified Callaway method developed by Morelli *et al.*,³⁰ hereafter referred to as the MHS model. The calculated values for bulk total thermal conductivity as well as the constituent thermal conductivities of phonons, electrons, holes, and bipolar diffusion are shown in Fig. 4 along with the experimental data of Gallo *et al.*¹ for bulk Bi.

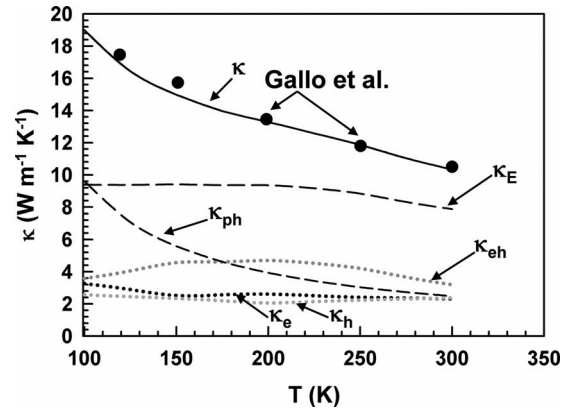


FIG. 4. Calculated thermal conductivity of bulk Bi perpendicular to the trigonal axis as well as the individual contributions of phonons, electrons, holes, and bipolar diffusion. Symbols are experimental values taken from Ref. 1.

After calibrating the bulk electronic and lattice thermal conductivity models with the reported bulk thermal conductivity, the lattice thermal conductivity of the NW, $\kappa_{ph,NW}$, is calculated using the MHS model. The bulk phonon dispersion relation^{31,32} was used in the model because recent results have suggested that the sound velocity of acoustic phonons in 200 nm Bi NWs is similar to that found in bulk polycrystalline Bi.³³ The boundary scattering mean free time $\tau_{ph,B}$ for a given phonon mode in a NW is obtained as $\tau_{ph,B}^{-1} = v/l_{ph,B}$, where $l_{ph,B}$ is the phonon boundary scattering mean free path and v is the phonon velocity for either the longitudinal or transverse phonon mode as given by the dispersion relation.³⁰ For a NW of diameter d , the value of $l_{ph,B}$ is given by^{34,35}

$$l_{ph,B} = \frac{1 + p_{ph}}{1 - p_{ph}} d, \quad (2)$$

where p_{ph} is the phonon-surface specularity parameter that represents the probability of specular scattering; specifically, a value of 1 corresponds to completely specular reflection, 0 indicates completely diffuse scattering, and values in between describe partially diffuse, partially specular scattering.³⁴

Figure 5 shows the calculated lattice thermal conductivity of a single-crystal Bi NW with the same growth direction and core diameter as NW3 for the two limiting cases of $p_{ph}=0$ and $p_{ph}=1$. The calculated lattice thermal conductivity for the diffuse surface case is not drastically lower than the specular surface scattering case, suggesting that the NW core diameter of 219 nm is not small enough to cause much suppression of the bulk phonon mean free path, which we calculate to be ~ 150 nm at 300 K based on the empirical relation reported by White and Woods.³⁶ We note that the measured total thermal conductivity of the NW is a factor of 3 lower than the lattice thermal conductivity in bulk Bi at 100 K. In addition, the measured total thermal conductivity is lower than the calculated lattice thermal conductivity for the diffuse case at temperatures lower than 225 K. This apparent discrepancy suggests that the observed reduction in the thermal conductivity cannot be attributed to diffuse phonon-surface scattering alone, and can have other origins.

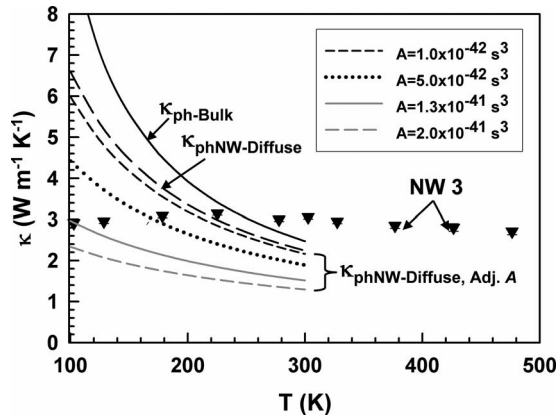


FIG. 5. Comparison of the measured thermal conductivity of NW3 with the calculated lattice thermal conductivity for specular (dark solid line) and diffuse (other lines) surface scattering. Unless noted in the figure, the impurity scattering parameter $A=0$.

We first consider contact thermal resistance as one possible reason for the measured thermal conductivity being lower than the calculated lattice thermal conductivity. Because electrical contact was not made to the NW, we could not employ a four-probe thermoelectric measurement method^{37,38} developed recently to measure the contact resistance directly. For CrSi₂ NWs with Pt-C deposited at the contacts in a similar fashion as the current work and Bi₂Te₃ NWs without Pt-C deposited at the contacts, the contact thermal resistance was found to be less than 10% of the measured total resistance. For Bi NW3, we calculate the contact thermal resistance according to a method reported recently,^{39,40} which is described in the supplemental materials.²⁴ The calculation result suggests that the contact thermal resistance is below 2% of the measured thermal resistance. Hence, the observed thermal conductivity suppression cannot be explained by the contact resistance alone.

Next, we consider the presence of a higher concentration of point defects or nonisotope impurity scattering in the NW than in the bulk. These two scattering processes are not considered in the MHS model.³⁰ Although NW3 was found to be single crystal based on the diffraction pattern taken with a 2 μm size electron beam, it could contain more impurities and point defects than bulk Bi crystal because of the synthesis process and conditions. Because graphite and residual air molecules were present in the vacuum-pumped growth apparatus, it is possible that the NW contains much higher carbon (C) or oxygen (O) impurities than bulk bismuth crystals. For the lattice thermal conductivity, the effects of point defect and nonisotope impurity scattering is accounted for by including an expression from the original Callaway model,⁴¹ which gives the phonon mean free scattering time due to impurities, $\tau_{i,\text{ph}}$, as $\tau_{i,\text{ph}}^{-1} = A\omega^4$ with ω being the phonon frequency and A an adjustable parameter.³⁰ With these modifications, the calculated lattice thermal conductivity becomes smaller than the measured thermal conductivity at 100 K when A is larger than $1.3 \times 10^{-41} \text{ s}^3$.

We next investigate the impurity or defect concentration c that could result in the obtained A values. For simplicity, we examine the case of substitutional impurity doping and take into account impurity scattering due to size difference-

induced local strain fields and mass difference between the impurity and the Bi atoms, which leads to^{41,42}

$$A \approx c \frac{3V^2}{\pi v_{\text{avg}}^3} \left[\left(\frac{1}{2\sqrt{3}} \frac{M_{\text{imp}} - M}{M} \right)^2 + \left(-3.2 \sqrt{\frac{2}{3}} \gamma \frac{R_{\text{imp}} - R}{R} \right)^2 \right], \quad (3)$$

where V is the volume per Bi atom, γ is the Grüneisen parameter, v_{avg} is the phonon velocity averaged between the three branches, M is the average mass of a Bi atom, R is the atomic radii of a Bi atom, M_{imp} is the average mass of the impurity atom, and R_{imp} is the atomic radii of the impurity atom. For impurities with small masses and sizes such as C, O, or copper (Cu), impurity concentrations in the 2.8×10^{19} to $2.0 \times 10^{20} \text{ cm}^{-3}$ range correspond to $A = 1.3 \times 10^{-41} \text{ s}^3$. If the impurities are mainly heavy atoms such as lead (Pb) where the mass and size differences from Bi are very small, a much higher concentration is needed to yield $A = 1.3 \times 10^{-41} \text{ s}^3$. We note that the obtained impurity concentrations are expected to be an upper bound to the actual case because no change in elastic constants between the impurity and the Bi host is accounted for. In addition, interstitial or void point defects can be more effective in scattering phonons and could lead to the same A value at a lower concentration than substitutional impurities.

Based on the calculated $\kappa_{\text{ph,NW}}$ curves and the measurement data for NW3, we evaluate the upper and lower bounds on the NW electronic thermal conductivity, $\kappa_{E,\text{NW}}$. We consider first the upper bound on the electronic thermal conductivity; this occurs where the lattice contribution is negligible such that the thermal transport is entirely electronic, i.e., $\kappa_{\text{NW}} = \kappa_{E,\text{NW}}$. By examining Fig. 4, it can be seen that the bulk electronic thermal conductivity κ_E is about three times higher than the measured total thermal conductivity of NW3. Thus, thermal transport by charge carriers in NW3 has been suppressed with the electronic thermal conductivity being reduced by at least a factor of 3. We then consider the case of the largest possible lattice thermal conductivity in NW 3 such that $\kappa_{\text{NW}} = \kappa_{\text{ph,NW}}$ at 100 K. This situation is depicted as the curve in Fig. 5 for diffuse surface scattering and $A = 1.3 \times 10^{-41} \text{ s}^3$, which gives a lower bound on the NW electronic thermal conductivity corresponding to the upper bound on the NW lattice thermal conductivity. Subtracting the calculated lattice thermal conductivity from the measured data gives a room temperature value of $\kappa_{E,\text{NW}} = 1.89 \text{ W/m K}$, four times smaller than the bulk κ_E . Thus, we conclude that the electronic thermal conductivity of the NW is three to four times smaller than found in bulk Bi in the same crystal direction.

We next investigate the origins of the suppressed electronic thermal conductivity. If the carrier concentrations and the electron-hole mobility ratio are the same in the NW as in bulk crystals, the suppressed electronic thermal conductivity corresponds to a 3–4 fold decrease in the electron and hole mobilities. The mobility of electrons and holes within the NW can be calculated using Matthieson's rule according to

$$\mu_{e,NW}^{-1} = \mu_e^{-1} + \mu_{e,B}^{-1} + \mu_{e,i}^{-1} \quad (4)$$

and

$$\mu_{h,NW}^{-1} = \mu_h^{-1} + \mu_{h,B}^{-1} + \mu_{h,i}^{-1}, \quad (5)$$

where $\mu_{e,NW}$ and $\mu_{h,NW}$ are the electron and hole NW mobilities, respectively, and μ_e and μ_h are the bulk electron and hole mobilities, respectively. The terms $\mu_{e,i}$ and $\mu_{h,i}$ are the mobility correction terms accounting for possibly higher impurity and defect concentrations in the NW than already accounted for within the bulk mobilities. The terms $\mu_{e,B}$ and $\mu_{h,B}$ are the electron and hole boundary scattering mobilities given by

$$\mu_{e,B} = \frac{e l_{eB}}{m_e^* v_{eF}} \quad (6)$$

and

$$\mu_{h,B} = \frac{e l_{hB}}{m_h^* v_{hF}}, \quad (7)$$

where m_e^* and m_h^* are the electron and hole conduction effective masses, v_{eF} and v_{hF} are the electron and hole Fermi velocities, and l_{eB} and l_{hB} are the adjustable electron and hole boundary scattering mean free paths, respectively. If all of the mobility reduction is the result of boundary scattering in the NW, the observed 3–4-fold decrease in mobilities in NW3 compared to the bulk requires $l_{eB} \sim 135\text{--}200$ nm and $l_{hB} \sim 195\text{--}295$ nm, both of which are close to the diffuse surface limit given by the NW core diameter of 219 nm.

However, we need to take into account a possibly higher impurity scattering rate ($\tau_{i,eh}^{-1}$) of electrons and hole in the NW because of a likely higher ionized impurity concentration (N_i). The mean free scattering time due to ionized impurities, $\tau_{i,eh}^{-1}$, is given by the Brooks-Herring formula as³⁴

$$\mu_{e,i} = \frac{2^{7/2}}{\pi^{3/2}} \frac{\varepsilon^2}{Z^2 e^3 m_e^{*1/2}} \frac{(k_B T)^{3/2}}{N_i} \left[\ln \left(1 + \frac{8 m_e^* 3 k_B T}{q^2 \hbar^2} \right) - \left(\frac{q^2 \hbar^2}{8 m_e^* 3 k_B T} \right)^{-1} \right], \quad (8)$$

$$\mu_{h,i} = \frac{2^{7/2}}{\pi^{3/2}} \frac{\varepsilon^2}{Z^2 e^3 m_h^{*1/2}} \frac{(k_B T)^{3/2}}{N_i} \left[\ln \left(1 + \frac{8 m_h^* 3 k_B T}{q^2 \hbar^2} \right) - \left(\frac{q^2 \hbar^2}{8 m_h^* 3 k_B T} \right)^{-1} \right], \quad (9)$$

where ε is the dielectric constant of Bi (taken to be $99.6\varepsilon_0$ from Ref. 43), Z is the valence difference between the impurity atom and Bi, m_e^* and m_h^* are the electron and hole conduction effective masses, respectively, and q is the screening radius (taken to be ~ 35 nm from Refs. 44–46).

Taking into account both surface scattering and impurity scattering of electrons, holes, and phonons, we calculate the NW values of κ_E , κ_{ph} , and κ for the case that the impurity doping is either fully ionized, substitutional O or C atoms. We assume that phonon scattering by the NW surface is diffuse because the surface roughness on the NW is comparable to or larger than the dominant phonon wavelength on the

order of 1 nm in the temperature range. On the other hand, the de Broglie wavelength of 5–50 nm for the charge carriers can be larger than the dominant phonon wavelength or the surface roughness because of the small effective mass in Bi along certain crystallographic directions. Hence, we have used the same specular parameter (p_{eh}) for electrons and holes as an adjustable parameter with the impurity concentration as an adjustable parameter. The Fermi level E_F was adjusted in the model according to the impurity concentration. The two fitting parameters (c and p_{eh}) are adjusted until the calculated κ fits with the measured κ of NW3. Based on the assumption of a given impurity type and diffuse phonon-surface scattering, there is little ambiguity in regards to fitting the measurement results at different temperatures. The lattice component of the thermal conductivity dominates at low temperatures, so the impurity concentration c is effectively set by matching the data points at temperatures near 100 K. The electronic part mainly determines the trend close to 300 K, so the charge carrier specular parameter is adjusted to best match those data points. Further details of this calculation can be found in the supplemental materials.²⁴ The obtained calculation results shown in Fig. 3 are for both C and O with $N_i = c = 2.8 \times 10^{19}$ cm⁻³, $p_{ph} = 0$ for diffuse phonon scattering and $p_{eh} = 0.25$ for partially diffuse scattering of electrons and holes. Because the two impurity types we consider (O and C) are similar in size and mass, the data may be acceptably fit with almost the exact same values c and p_{eh} . If the dominant impurity atoms are very different in size and mass from C and O, other values of c and p_{eh} would be obtained. In addition, if the difference in elastic constants between Bi and the impurity atom were accounted for in the phonon-impurity scattering analysis, the value of c would be smaller and the specular parameter for charge carriers would be reduced in order to fit the same data set. Despite the uncertainty in the impurity type and the inaccuracy in the phonon-impurity scattering model, the calculation shows that a combination of surface scattering of phonons and charge carriers and an impurity concentration on the order of 10^{19} cm⁻³ is sufficient to cause the observed reduced κ of the single-crystal NW3.

For the case of polycrystalline NWs, the boundary scattering mean free paths for phonons and charge carriers can be smaller than the NW diameter due to the presence of grain boundaries. For NW2, NW4, and NW6, the measured thermal conductivity values can be fit using phonon boundary scattering mean free paths of 15–40 nm and charge carrier-boundary scattering mean free paths of 25–40 nm (Fig. 3) using the same impurity concentration found above from NW3. In comparison, a phonon mean free path of 11.8 nm was estimated for nanoporous Bi thin films based on measurements of the cross-plane thermal conductivities in the range of 0.08–0.8 W/m K.⁴⁷ Moreover, the comparable thermal conductivity values measured for the polycrystalline NW samples of varying diameters illustrate that grain boundary scattering dominates over surface scattering in the NWs. Hence, the measurement results suggest that the thermal conductivity can be suppressed more effectively by grain boundary scattering than surface scattering. In fact, effective pho-

non scattering at grain boundaries has recently been employed as a means of increasing ZT in nanocomposite bulk thermoelectric materials.⁴⁸

V. CONCLUSION

This measurement shows that the thermal conductivity of a single crystal and several polycrystalline Bi NWs are suppressed below those of bulk Bi single crystal. The total thermal conductivity of the single-crystal NW of 232 nm diameter is suppressed from the bulk value in the same direction perpendicular to the trigonal axis by factors of 3–6 over the temperature range of 100–300 K. The electronic thermal conductivity of this NW is found to be suppressed to three to four times smaller than that calculated for bulk Bi. The suppression in the single-crystal NW can be explained by a transport model that considers diffuse phonon-surface scattering, partially diffuse surface scattering of electrons and holes, and scattering of phonons and charge carriers by ionized impurities such as O and C with a concentration on the order of 10^{19} cm⁻³. The thermal conductivity values measured for polycrystalline NW samples of varying diameter between 74 and 255 nm are 3–13 times lower than that found for the single-crystal NW, and do not show apparent diameter dependence. The grain boundary scattering mean free path for all heat carriers are determined to be in the range of 15–40 nm in the polycrystalline NWs, suggesting that grain boundary scattering dominates over surface scattering for these NWs.

ACKNOWLEDGMENTS

This work is supported, in part, by the Office of Naval Research (Program Manager: Dr. Mihai E. Gross), the National Science Foundation (Thermal Transport Processes Program), and DARPA Advanced Processing and Prototyping Center.

¹C. F. Gallo, B. S. Chandrasekhar, and P. H. Sutter, *J. Appl. Phys.* **34**, 144 (1963).

²R. Hartman, *Phys. Rev.* **181**, 1070 (1969).

³J. Heremans and O. P. Hansen, *J. Phys. C* **12**, 3483 (1979).

⁴X. Sun, Z. Zhang, and M. S. Dresselhaus, *Appl. Phys. Lett.* **74**, 4005 (1999).

⁵Y.-M. Lin, X. Sun, and M. S. Dresselhaus, *Phys. Rev. B* **62**, 4610 (2000).

⁶D. M. Rowe, *CRC Handbook of Thermoelectrics* (CRC, Boca Raton, FL, 1994).

⁷D. Li, S. Huxtable, A. Abramson, and A. Majumdar, *ASME J. Heat Transfer* **127**, 108 (2005).

⁸L. D. Hicks and M. S. Dresselhaus, *Phys. Rev. B* **47**, 16631 (1993).

⁹L. D. Hicks, T. C. Harman, and M. S. Dresselhaus, *Appl. Phys. Lett.* **63**, 3230 (1993).

¹⁰L. D. Hicks and M. S. Dresselhaus, *Phys. Rev. B* **47**, 12727 (1993).

¹¹Y. Liu and R. E. Allen, *Phys. Rev. B* **52**, 1566 (1995).

¹²A. Boukai, K. Xu, and J. R. Heath, *Adv. Mater. (Weinheim, Ger.)* **18**, 864 (2006).

¹³O. Rabina, Y.-M. Lin, and M. S. Dresselhaus, *Appl. Phys. Lett.* **79**, 81 (2001).

¹⁴G. Chen and A. Shakouri, *ASME J. Heat Transfer* **124**, 242 (2002).

¹⁵J. Heremans, C. M. Thrush, Y.-M. Lin, S. Cronin, Z. Zhang, M. S. Dresselhaus, and J. F. Mansfield, *Phys. Rev. B* **61**, 2921 (2000).

¹⁶D. Li, Y. Wu, P. Kim, L. Shi, P. Yang, and A. Majumdar, *Appl. Phys. Lett.* **83**, 2934 (2003).

¹⁷L. Shi, Q. Hao, C. Yu, N. Mingo, X. Kong, and Z. L. Wang, *Appl. Phys. Lett.* **84**, 2638 (2004).

¹⁸C. Guthy, C.-Y. Nam, and J. E. Fischer, *J. Appl. Phys.* **103**, 064319 (2008).

¹⁹H. Masuda and M. Satoh, *Jpn. J. Appl. Phys., Part 2* **35**, L126 (1996).

²⁰T. Xu, R. Piner, and R. Ruoff, *Langmuir* **19**, 1443 (2003).

²¹S. B. Cronin, Y.-M. Lin, O. Rabin, M. R. Black, J. Y. Ying, M. S. Dresselhaus, P. L. Gai, J.-P. Minet, and J.-P. Issi, *Nanotechnology* **13**, 653 (2002).

²²S. B. Cronin, Y.-M. Lin, M. R. Black, O. Rabin, and M. S. Dresselhaus, *Proceedings of the 21st International Conference on Thermoelectrics* (IEEE, Long Beach, CA, 2002), p. 243.

²³L. Shi, D. Li, C. Yu, W. Jang, Z. Yao, P. Kim, and A. Majumdar, *ASME J. Heat Transfer* **125**, 881 (2003).

²⁴See EPAPS supplementary material at [10.1063/1.3191657](http://dx.doi.org/10.1063/1.3191657) for additional description of the measurement and calculation methods and results.

²⁵G. A. Slack, in *Solid State Physics*, edited by H. Ehrenreich, F. Seitz, and D. Turnbull (Academic, New York, 1974), Vol. 34, p. 1.

²⁶C. Uher and H. J. Goldsmid, *Phys. Status Solidi* **65**, 765 (1974) (b).

²⁷G. E. Smith, *Phys. Rev. Lett.* **9**, 487 (1962).

²⁸R. T. Isaacson and G. A. Williams, *Phys. Rev.* **185**, 682 (1969).

²⁹J.-P. Michenaud and J.-P. Issi, *J. Phys. C* **5**, 3061 (1972).

³⁰D. T. Morelli, J. P. Heremans, and G. A. Slack, *Phys. Rev. B* **66**, 195304 (2002).

³¹J. L. Yarnell, J. L. Warren, R. G. Wenzel, and S. H. Koenig, *IBM J. Res. Dev.* **8**, 234 (1964).

³²E. D. Murray, S. Fahy, D. Prendergast, T. Ogitsu, D. M. Fritz, and D. A. Reis, *Phys. Rev. B* **75**, 184301 (2007).

³³A. A. Kolomenskii, S. N. Jerebtsov, H. Liu, H. Zhang, Z. Ye, Z. Luo, W. Wu, and H. A. Schuessler, *J. Appl. Phys.* **104**, 103110 (2008).

³⁴J. M. Ziman, *Electrons and Phonons: The Theory of Transport Phenomena in Solids* (Clarendon, Oxford, 1962).

³⁵C. Dames and G. Chen, *J. Appl. Phys.* **95**, 682 (2004).

³⁶G. K. White and S. B. Woods, *Philos. Mag.* **3**, 342 (1958).

³⁷A. Mavrokefalos, M. T. Pettes, F. Zhou, and L. Shi, *Rev. Sci. Instrum.* **78**, 034901 (2007).

³⁸F. Zhou, J. Szczech, M. T. Pettes, A. L. Moore, S. Jin, and L. Shi, *Nano Lett.* **7**, 1649 (2007).

³⁹C. Yu, S. Saha, J. Zhou, L. Shi, A. M. Cassell, B. A. Cruden, Q. Ngo, and J. Li, *ASME J. Heat Transfer* **128**, 234 (2006).

⁴⁰R. Prasher, *Phys. Rev. B* **77**, 075424 (2008).

⁴¹J. Callaway, *Phys. Rev.* **113**, 1046 (1959).

⁴²P. G. Klemens, *Proc. Phys. Soc. A* **68**, 1113 (1955).

⁴³W. S. Boyle and A. D. Brailsford, *Phys. Rev.* **120**, 1943 (1960).

⁴⁴J. D. H. Brownell and E. H. Hygh, *Phys. Rev.* **164**, 916 (1967).

⁴⁵V. T. Petrashov, V. N. Antonov, and B. Nilsson, *J. Phys.: Condens. Matter* **3**, 9705 (1991).

⁴⁶V. Sandomirsky, A. V. Butenko, R. Levin, and Y. Schelsinger, *J. Appl. Phys.* **90**, 2370 (2001).

⁴⁷D. W. Song, W.-N. Shen, B. Dunn, C. D. Moore, M. S. Goorsky, T. Radetic, R. Gronsky, and G. Chen, *Appl. Phys. Lett.* **84**, 1883 (2004).

⁴⁸B. Poudel, Q. Hao, Y. Ma, Y. Lan, A. Minnich, B. Yu, X. Yan, D. Wang, A. Muto, D. Vashaee, X. Chen, J. Liu, M. S. Dresselhaus, G. Chen, and Z. Ren, *Science* **320**, 634 (2008).